

Extreme Mechanical Behavior of Nacre-Mimetic Graphene-Oxide and Silk Nanocomposites

Wanting Xie,^{†,‡,§} Sirimuvva Tadepalli,[§] Sang Hyun Park,[§] Amir Kazemi-Moridani,[‡] Qisheng Jiang,[§] Srikanth Singamaneni,^{*,§,§} and Jae-Hwang Lee^{*,‡,§}

[†]Department of Physics, University of Massachusetts Amherst, Amherst, Massachusetts 01003, United States

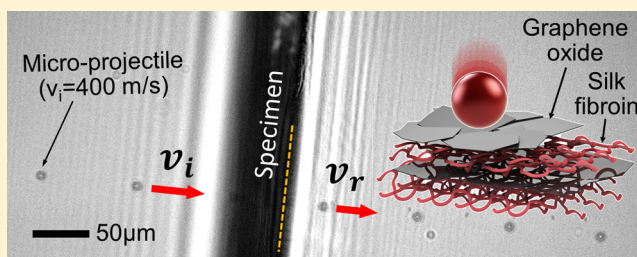
[‡]Department of Mechanical and Industrial Engineering, University of Massachusetts Amherst, Amherst, Massachusetts 01003, United States

[§]Department of Mechanical Engineering and Materials Science and Institute of Materials Science and Engineering, Washington University in St. Louis, St. Louis, Missouri 63130, United States

Supporting Information

ABSTRACT: Biological materials have the ability to withstand extreme mechanical forces due to their unique multilevel hierarchical structure. Here, we fabricated a nacre-mimetic nanocomposite comprised of silk fibroin and graphene oxide that exhibits hybridized dynamic responses arising from alternating high-contrast mechanical properties of the components at the nanoscale. Dynamic mechanical behavior of these nanocomposites is assessed through a microscale ballistic characterization using a 7.6 μm diameter silica sphere moving at a speed of approximately 400 m/s. The volume fraction of graphene oxide in these composites is systematically varied from 0 to 32 vol % to quantify the dynamic effects correlating with the structural morphologies of the graphene oxide flakes. Specific penetration energy of the films rapidly increases as the distribution of graphene oxide flakes evolves from noninteracting, isolated sheets to a partially overlapping continuous sheet. The specific penetration energy of the nanocomposite at the highest graphene oxide content tested here is found to be significantly higher than that of Kevlar fabrics and close to that of pure multilayer graphene. This study evidently demonstrates that the morphologies of nanoscale constituents and their interactions are critical to realize scalable high-performance nanocomposites using typical nanomaterial constituents having finite dimensions.

KEYWORDS: Scalable nanocomposite, penetration dynamics, high strain rate, flexible armor



Nanocomposites comprised of materials with distinct mechanical properties and tailored interfaces between the components have received wide attention over the last two decades due to their synergistically improved properties compared to the individual components.^{1–3} Nanocomposites are promising for the development of lightweight ballistic armor materials, where dissipation of a projectile's massive kinetic energy with a limited areal density (or mass per unit area) is required. In contrast to conventional structural composites being used below a material's yield strength, due to the extreme nature of mechanical interactions between a high-speed projectile and an armor composite, irreversible structural damage via dynamic failure processes including cracking, fragmentation, shear, and delamination are generally accompanied.⁴ In this aspect, typical composites that have micro- or larger scale material phases still tend to exhibit characteristic failure mechanisms of individual constituent materials because a material's intrinsic failure mechanism is governed at the submicrometer scale. Therefore, in addition to the superior load transfer efficiency, which is attributed to the large interfacial area between phases,⁵ composites with

nanoscale phases or nanocomposites exhibit a hybridized failure mechanism for enhanced antiballistic performance.

As a filler for nanocomposites, graphene oxide (GO) stands out among reinforcing nanofiller materials due to its attractive characteristics, including high elastic modulus (250 GPa),⁶ low density,⁷ high water solubility, and good mechanical flexibility.⁸ As a matrix, we employed silk fibroin (SF), a material that forms one of the toughest natural fibers, as well as a good candidate for both a binder and matrix.^{9–12} Both components of the nanocomposite are amphiphilic, GO comprised of hydrophobic graphitic and hydrophilic oxidized functionalities; SF also contains both hydrophilic and hydrophobic domains.¹³ The complementary heterogeneity of GO and SF can maximize various noncovalent interactions between the fillers and the matrix. The mechanical performance of materials largely depends on the interactions at the interface, so maximizing

Received: October 16, 2017

Revised: December 19, 2017

Published: January 9, 2018

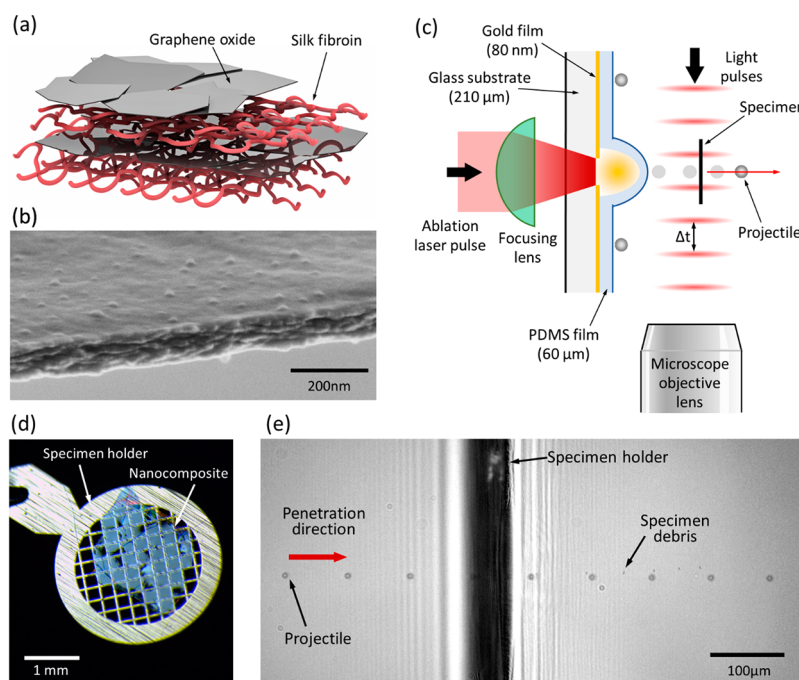


Figure 1. (a) Illustration of LbL assembled GO-SF nanocomposite depicting the brick and mortar structure. (b) SEM of a 150 nm thick GO-SF film. (c) Schematic illustration of the α -LIPIT experiment. (d) A GO-SF film suspended on a TEM grid. (e) Penetration micrograph recorded by multiple exposures. The straight fringes along the specimen holder are due to optical diffraction of illumination pulses.

the interfacial binding is critical for achieving desired mechanical properties.¹³

GO-SF nanocomposite membranes were fabricated by a spin-assisted layer-by-layer (SA-LbL) assembly of GO and SF solutions (Figure 1a). SA-LbL offers a precise control over the composition, thickness of the individual components and the composite, and a highly stratified structure along the thickness.¹⁴ Owing to the highly stratified nature of the composites, SA-LbL has been extensively utilized for the fabrication of nacre-mimetic composites.^{15–17} In previous studies, the GO-SF composite membranes showed promising mechanical properties (modulus of 145 GPa, ultimate stress of above 300 MPa, toughness of above 2.2 MJ m⁻³) as a result of the formation of strong molecular interphase zones.^{18–23} Dynamic SA-LbL assembly (170 GPa, 300 MPa, 3.4 MJ m⁻³) and water vapor annealing (105 GPa, 460 MPa, 2.1 MJ m⁻³) were introduced to further improve the mechanical characteristics of GO-SF.^{24,25} The combination of GO and SF forms a nacre-like “brick-and-mortar” arrangement,^{26,27} known for its remarkable strength and toughness.^{28–31} A recent simulation study on multilayer-graphene/poly(methyl methacrylate) nanocomposites reveals two deformation and failure mechanisms, yielding failure within graphene and pull-out failure along the interface.^{32,33} According to the authors, there is more energy dissipation per layer through multilayer-graphene yielding than pull-out, implying that the staggered architecture is more critical in the mechanical performance than the interfacial interaction strength.

Despite immense efforts dedicated to the design and fabrication of graphene-based nanocomposites, their mechanical behavior is not studied under high strain rate (HSR), especially at a deformation speeds comparable to supersonic muzzle velocities. Unlike quasi-static conditions, in which load can be transferred through dynamic friction at interfaces by relative sliding between sheets,^{32,33} HSR inelastic material behavior is substantially different due to the wave propagation,

inertia effect, and the adiabatic process.³⁴ Therefore, HSR mechanical characterization is of great significance for the development of armor materials based on nanocomposites. Several techniques were used to study material behavior at HSRs, such as dropweight machine,³⁵ split Hopkinson pressure bars,³⁶ Taylor impact,³⁷ and plate impact.³⁸ However, as all these techniques require a macroscopic sample and it is challenging to apply these HSR mechanical characterization techniques to nanocomposites as shown in the scanning electron micrograph (SEM) (Figure 1b and Figure S3). Thus, we have employed an advanced laser-induced projectile impact test (α -LIPIT) (Figure 1c) to investigate the armor characteristics of GO-SF nanocomposites membranes.^{39–41} The GO-SF membrane was transferred onto an 80-mesh Transmission electron microscope (TEM) grid (200 μ m square hole). As a projectile, a single solid silica microsphere $D = 7.62 \pm 0.22 \mu$ m was accelerated to approximately 400 m s⁻¹ and penetrated through a suspended GO-SF specimen (Figure 1d and Figure S2) in air. The positions of the projectile were quantified using a multiexposure ultrafast photograph, taken by 1 ps white-light pulses with an interpulse interval of 200 ns (Figure 1e).

Before proceeding the mechanical characteristics of GO-SF nanocomposites at HSRs, we investigated the structure and static mechanical properties of ultrathin nanocomposites with a special attention to the interfacial interactions between the two components. The nacre-like brick-and-mortar structure is known to be critical for the excellent mechanical properties of GO-SF nanocomposites.²⁵ It has been reported that the formation of molecular interphase zones contributes to the reinforcing effect of GO incorporated into SF matrix.²² We tuned the ionization state of SF chains by altering the pH of the solution. Oxidized domains of GO, therefore, repel negatively charged SF chains and push them toward the unoxidized hydrophobic domains, facilitating hydrophobic interactions and load transfer between the matrix and filler. According to a

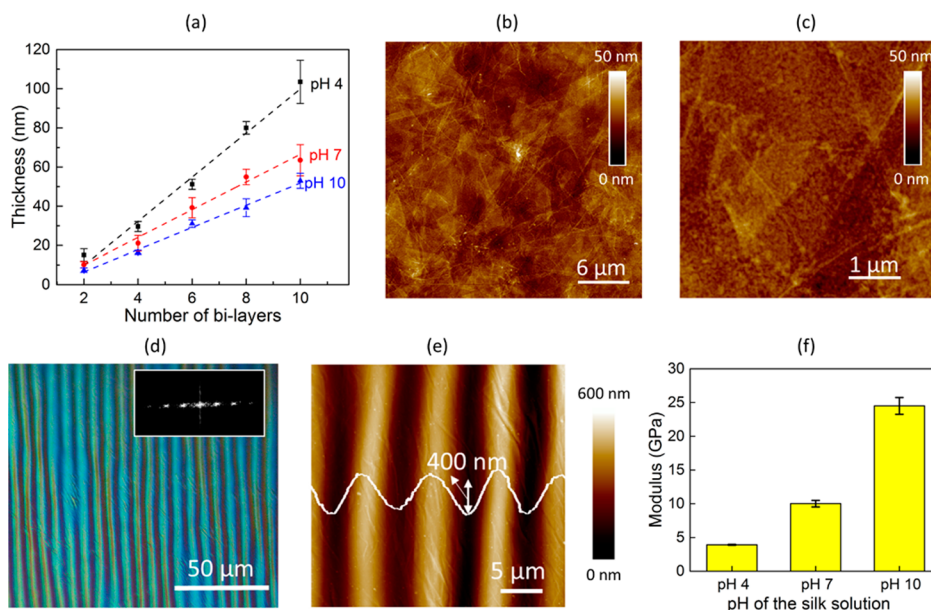


Figure 2. (a) Thickness of the GO-SF composite films as a function of number of bilayers fabricated using SF solutions of different pH. (b) Representative AFM height image of the GO-SF composite film surface. (c) Higher-magnification AFM image of the composite structure. (d) Optical micrograph of a buckled GO-SF film (pH 10). Inset showing a corresponding 1D-FFT pattern of the micrograph. (e) AFM image of the buckled GO-SF composite film (pH 10) on PDMS substrate under compression. (f) Elastic moduli of the GO-SF films fabricated using SF solutions at different pH.

previous study, there are more random coils and less β -sheets at higher pH.⁴² These amorphous SF chains act as linkers between β -sheet domains, leading to the larger shear strength. All these factors contribute to the mechanical responses of GO-SF membranes at HSRs.

In a previous study, we demonstrated that the interfacial interactions between GO and SF are highly dependent on the pH of the SF solution during adsorption.⁴² Because of the multidomain and amphiphilic nature of SF, the adsorption of SF on GO is influenced by the ionization state of the SF, which is governed by the pH of the solution. We fabricated GO-SF films using SA-LbL assembly. The composite films were comprised of ten bilayers of GO and SF. We adjusted the pH of the SF solution to pH 4, pH 7, and pH 10 during deposition to probe the effect of pH on the elastic modulus of the composite films with a GO content of 12.5 vol %. At pH 4, SF was positively charged resulting in favorable electrostatic interactions between GO and SF. In contrast, at pH 10, SF was strongly negatively charged resulting in hydrophobic interactions between GO and SF.⁴² Because of the pH-dependent GO-SF and intersilk interactions, the thickness of SF was found to be higher at pH 4 when compared to that at pH 7 (Figure 2a). The thickness of GO/SF bilayer at pH 10 was found to be ~ 5 nm, which agreed with the previously reported results, while the thickness of the bilayer at pH 4 is ~ 7.5 nm.²² Representative AFM (atomic force microscopy) images of the composite film (assembled at pH 10) revealed a uniform and dense coverage of GO flakes with an RMS roughness of 3.1 ± 1.9 nm over a $1 \times 1 \mu\text{m}$ area (Figure 2b,c).

In order to measure the static elastic modulus, we fabricated a free-standing GO-SF composite film using polystyrene as a sacrificial layer (see experimental section in SI for details). The ability to freely suspend the GO-SF film was demonstrated by transferring the film onto a TEM grid with $\sim 200 \mu\text{m}$ apertures. After transfer of the free-standing film onto a compliant polydimethylsiloxane (PDMS) substrate, the elastic modulus of

GO-SF film was determined using strain-induced elastic buckling instability technique.⁴³ Briefly, a compressive stress above certain threshold on a compliant material with a stiff skin layer results in spontaneous periodic buckling patterns in the film to minimize the strain energy.⁴⁴ The buckling wavelength is given by⁴⁵

$$\lambda = 2\pi t \left[\frac{(1 - \nu_s^2)E_f}{3(1 - \nu_f^2)E_s} \right]^{1/3}$$

where λ is the wavelength of the periodic buckling pattern, E_f and ν_f are the elastic modulus and the Poisson's ratio of the stiff skin layer respectively, E_s and ν_s are the elastic modulus and the Poisson's ratio of the compliant substrate, respectively, and t is a thickness of the stiff skin layer.

Compression of the compliant PDMS substrate with GO-SF film on the surface resulted in uniform buckling of the film (Figure 2d). A fast Fourier transformation (FFT) of the optical images was employed to determine the wavelength of the buckles to be $7.4 \pm 0.2 \mu\text{m}$ (inset of Figure 2d). AFM imaging of the buckled surface further confirmed the periodicity of the buckling patterns and revealed amplitude of the buckles to be ~ 400 nm (Figure 2e). The corresponding elastic modulus of the GO-SF film varied with the pH of the SF solution employed in LbL assembly. The elastic modulus of the GO-SF film assembled at pH 4 was found to be 4.8 ± 0.6 GPa, while those of the GO-SF film assembled at pH 7 and pH 10 were found to be 7.2 ± 0.3 and 26.6 ± 0.3 GPa, respectively. As reported in the previous study,⁴² the extent of β -sheet formation in GO-SF bilayered film was higher when assembled at pH 4 compared to that at pH 10. However, the lower modulus of the GO-SF bilayered film at pH 4 compared to that assembled at pH 10 can be attributed to the absence of intersilk repulsion at pH 4, resulting in clusters of SF on the GO flakes resulting in nonuniform packing and poor interfacial interaction between GO and SF (Figure S5). The weak interfacial

interactions between the SF and GO leads to poor stress transfer from SF matrix to GO and partial slippage of the GO flakes under compressive stress. Despite the lower β -sheet content in the GO-SF film assembled at pH 7 and pH 10, the SF chains uniformly distributed on the GO flakes and facilitated better interfacial interactions and packing, thus enhancing the elastic modulus of the composite film (Figure S7). The vast majority of fibrillar structures observed in at pH 7 and 10 were individual nanofibrils or limited multidomains, rather than bundles as usually observed for longer adsorption on hydrophilic substrates.⁴⁶ The absence of substantial aggregation and self-folding is critically important for maximizing interfacial interactions among different SF domains and GO surface.⁴⁷

To further understand the static mechanical properties of the GO-SF composites, we varied the GO content in the composite film by varying the concentration of GO used in the SA-LbL process and by altering the number of bilayers used in the GO-SF composite (see experimental details in SI). Composite films with a GO content of 0, 8, 25, and 32 vol % were achieved using SA-LbL process at pH 10. According to the morphology of the GO-SF composite, as the GO content increased, the roughness of the composite also increased, which indicated that the GO flakes start impinging upon one another at higher concentrations (Figure 3a–d). Increasing the GO content higher than 32 vol % in the composite resulted in a large overlap of the GO flakes and formation of GO multilayers. Using FFT of the optical images, the buckling wavelength and the elastic modulus of the GO-SF films were determined (Figure 2e). We found that increasing the GO content from 0 to 32 vol % in the composite film resulted in an increase in the elastic modulus from 4.1 ± 0.5 to 76.8 ± 9.1 GPa.

The reported value of the elastic modulus of GO is 207.6 ± 23.4 GPa while the elastic modulus of SF varies from 4 to 22 GPa depending on the ratio of the random coil to the β -sheet content.^{6,22} We modeled the elastic modulus of the GO-SF composites using the Halpin–Tsai model that is widely used to estimate mechanical properties of aligned linear-elastic orthotropic composites. The estimated elastic modulus according to the Halpin–Tsai model is expressed by⁴⁸

$$E_c = E_m \frac{(1 + \eta \xi V_f)}{(1 - \eta V_f)}$$

$$\eta = \frac{\left(\frac{E_f}{E_m} - 1\right)}{\left(\frac{E_f}{E_m} + \xi\right)}$$

where E_c , E_f , and E_m are the moduli of the composite, filler, and matrix, respectively, and V_f is the volume fraction of the filler. ξ is a shape parameter that depends on the filler geometry, orientation, and loading direction, and is given by the following equation⁴⁸

$$\xi = \frac{2l_f}{3t_f}$$

where l_f and t_f are the length and thickness of the GO flakes, respectively. The elastic modulus estimated by the Halpin–Tsai model linearly increased with an increase in the GO content. The experimentally obtained elastic moduli of the GO-SF composites agreed well with the theoretical values, predicted by the Halpin–Tsai model (Figure 3f). The highest elastic modulus of the GO-SF composite was found to be $76.8 \pm$

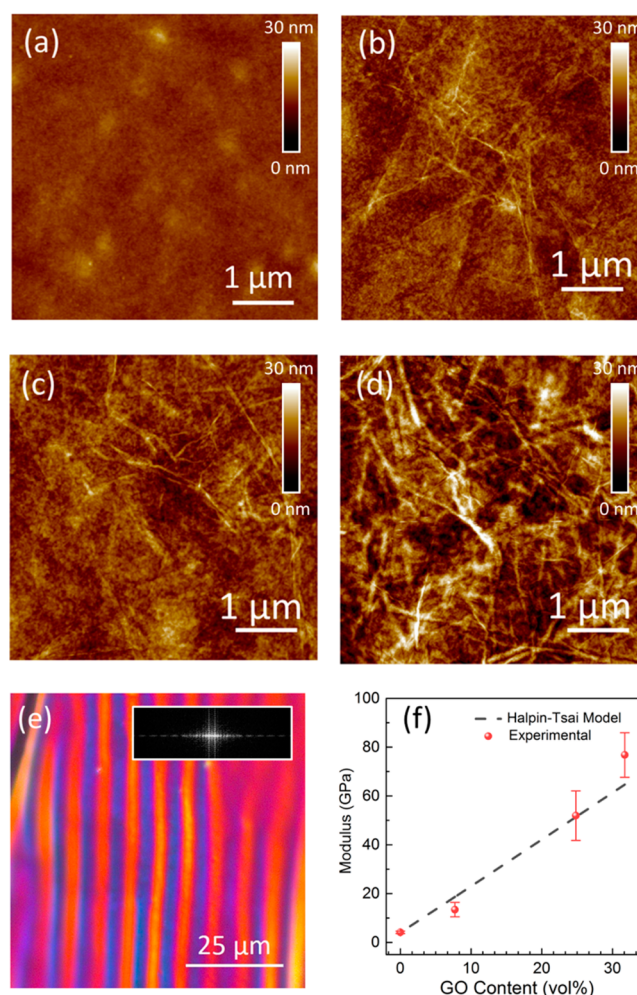


Figure 3. AFM images of the GO-SF composite films with different GO content (a) 0, (b) 8, (c) 25, and (d) 32 vol %. (e) Optical micrograph of a buckled GO-SF composite film on PDMS substrate. (f) Elastic moduli of the GO-SF films at different volume fractions of GO in the composites.

9.1 GPa despite having $\sim 70\%$ SF in the matrix. The dense network of weak interactions (hydrogen bonding, hydrophobic, and polar) between GO and SF are responsible for the synergistic enhancement in the elastic modulus due to the reinforcing effect of GO-SF interfacial interactions.

To investigate the effects of GO-content on the antiballistic armor characteristics of GO-SF nanocomposites, we tested the nanocomposite specimens, fabricated using SF solution at pH 10 with different GO volume fractions: pure SF, 8, 25, and 32 vol %, corresponding to approximately 0, 50, 75, and 100% areal coverage of GO flakes, respectively (Figure S6). Postpenetration optical micrographs showed a variation of major fracture characteristics depending on the GO volume fraction (Figure 4). The penetration holes of pure SF showed the average diameter of $5.6 \mu\text{m}$, closer to D , while considerably smaller hole diameters (3.0 , 3.3 , and $3.2 \mu\text{m}$ for 8, 25, and 32 vol %) were created in all GO-SF composites. In addition, 25 and 32 vol % composites consistently displayed more irregular penetration perimeters. These distinctive features support that the GO nanofiller enhances fracture toughness to a certain extent. Interestingly, longer radial cracks (an average of 10.7 , 9.1 , and $10.5 \mu\text{m}$ for 8, 25, and 32 vol %) (Figure 4b–d) were frequently observed in all nanocomposites, compared to the 2.9

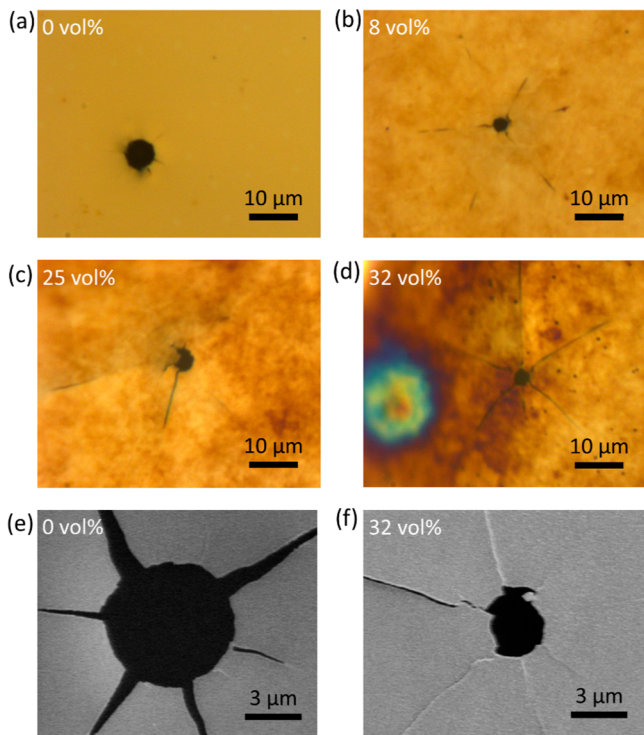


Figure 4. Postimpact optical micrographs of 150 nm thick films with different GO concentration, (a) 0, (b) 8, (c) 25, and (d) 32 vol %. SEM images of near impact sites of nanocomposites membranes of (e) 0 and (f) 32 vol % of GO concentration.

μm of pure SF (Figure 4a). One may understand that this is contradictory to the enhanced fracture toughness. However, as the enhanced toughness can delay the initiation of the radial cracks within the direct strike area, this delay can allow radial stress waves to propagate farther prior to penetration. Moreover, since the higher GO content also increases the effective propagation speed of the stress waves, a much wider region of the specimen can be under tensile stresses during the penetration event. Thus, we consider that the enhanced toughness and the faster speed of stress waves led to the longer radial cracks.

Because of the extremely light mass of the projectile ($m = 4.4 \times 10^{-13}$ kg), we were able to quantify instantaneous velocity, $v(t)$, and acceleration, $a(t)$, of the projectile, using the first and second derivative of the positions of a projectile, $z(t)$, respectively (Figure 5a). Thus, kinetic energy loss is defined by $\Delta E_k(t) = \frac{1}{2}m[v_i(0)^2 - v_i(t)^2]$, and the force exerted to the projectile is $F(t) = ma(t)$. The sudden jump in the force plot is obviously from the mechanical interaction between the specimen and the projectile, corresponding to a rapid increase of ΔE_k . In addition, the deceleration of the projectile by air drag can be clearly seen from the nonzero slope of ΔE_k prior and after penetration. Therefore, ΔE_k can be decomposed by

$$\Delta E_k = \frac{1}{2}m(v_i^2 - v_r^2) = E_p + E_{\text{air}} \quad (1)$$

where E_p is the net energy needed to penetrate a nanocomposite specimen and E_{air} is energy loss due to the air drag. Besides the projectile, debris from the specimen decelerated more significantly due to its lighter mass (Figure 1e). As a simplified model, we supposed that a fraction of E_p was caused by the kinetic energy transfer to the debris from the strike face

area of a specimen ($A_s = \pi D^2/4$). The rest of E_p is related to other delocalized dissipation mechanisms, which is denoted as E_d . Assuming an inelastic collision to a thin membrane ($D \gg h$), E_p is expressed by two terms

$$E_p = (\rho A_s h) \frac{v_i^2}{2} + E_d \quad (2)$$

where ρ is the density of the specimen and h is the specimen thickness. When introducing the specific penetration energy, E_p^* , defined by $E_p(\rho A_s h)^{-1}$, the characteristic antiballistic performance of materials can be compared regardless of material's areal density and a projectile diameter

$$E_p^* = \frac{v_i^2}{2} + E_d^* \quad (3)$$

E_d^* is the specific delocalized penetration energy showing the capability of a material to distribute the impact energy beyond the direct strike area while excluding material-independent term, $v_i^2/2$, caused by the kinetic energy transfer to the material within the direct strike area.⁴⁰

For the films with thicknesses ranging from 80 to 150 nm, E_p^* values of different GO-SF composites (Figure 5b) were quantified from the slope of $E_p(h)$ upon testing specimens with two different thicknesses (see Figure S4). Note that for each thickness, a total of 10 independent microballistic characterizations were performed and the error bar was the standard deviation of linear fitting using the total 20 measured values of ΔE_k . The E_p^* value of pure SF is 0.42 MJ kg^{-1} while 8 vol % GO sample showed only a slight improvement (<5%) in the E_p^* values as the nanocomposite has silk as the major component (92%) for load transfer. The E_p^* values of 25 vol % GO sample increases by 26%, compared to pure SF suggesting that the GO flakes significantly influence the load transfer mechanism. E_p^* increased monotonically with higher GO-content, due to the enhanced fracture toughness and faster propagation of stress waves. Unexpectedly, E_p^* revealed an onset of a new behavior between 25 and 32 vol %, which is distinguished from the trend originated from the stochastic nature of GO-SF composite morphology. We believe that the onset of the transition is due to the complete coverage of GO flakes resulting in overlapped GO flakes rather than being isolated from other GO flakes. Because of the partially overlapping GO flakes, radial stress waves can propagate significantly farther through the composite since the in-plane speed of sound of GO flakes can be considerably faster than that of SF due to higher Young's modulus of GO ($E_{\text{GO}} \sim 207.6 \text{ GPa}$)⁶ than that of SF ($E_{\text{SF}} \sim 4.1 \text{ GPa}$), where the speeds of sound is proportional to \sqrt{E} . Therefore, the abrupt increase at 100% areal coverage can be accredited to the impact energy delocalization by the elastic wave propagation through the connected GO flakes.⁴⁹

E_d^* , the difference between E_p^* and $v_i^2/2$, indicates how efficiently the material can dissipate penetration energy through the delocalization process along the in-plane direction. Because this redirection of energy flow from the normal to tangential direction is highly desired in an armor to achieve the same antiballistic performance with less material, E_p^* of pure SF and GO-SF composites were compared with other microscopic and macroscopic materials from previous literature (Figure 5c).⁴⁰ Note that the chart is intended to provide the current status of nanomaterials' performance at the microscale in comparison to the performance of macroscopic materials although the

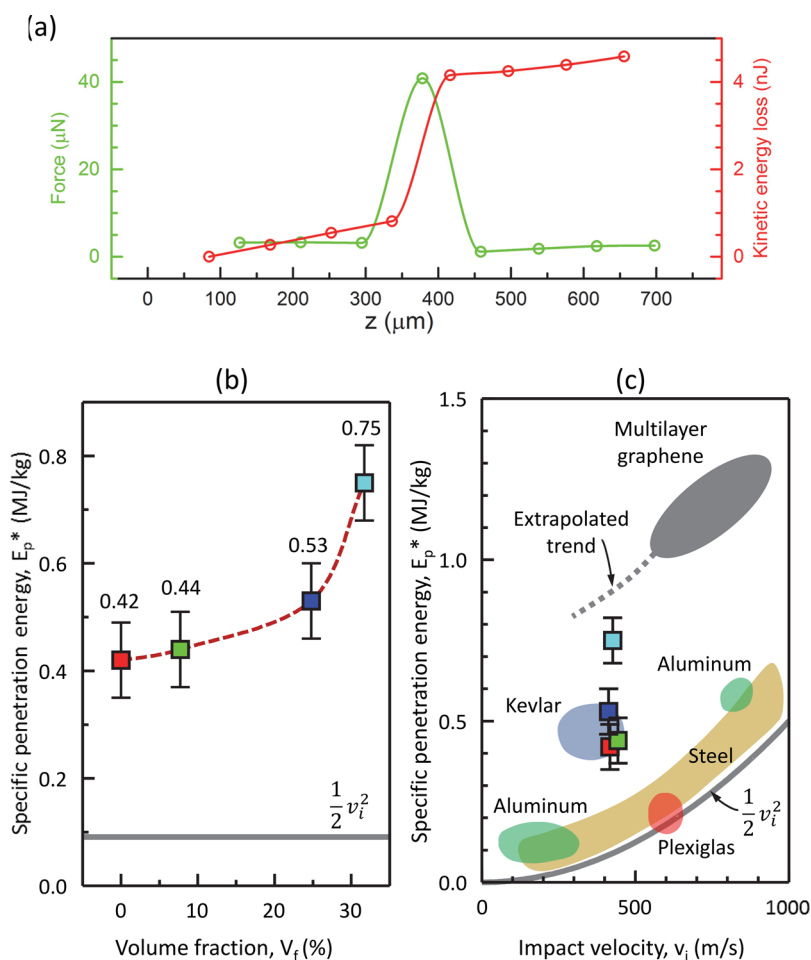


Figure 5. (a) Force and kinetic energy loss during the penetration process. (b) Specific penetration energy of GO-SF composites with different GO volume fraction. (c) Specific penetration energy of GO-SF composites compared with several other materials.

quantitative correspondence between microscopic and macroscopic ballistic results may need a more comprehensive investigation. The three lower concentration materials displayed antiballistic characteristics similar to Kevlar, a very popular armor material, and superior over ductile metals (aluminum and steel) and amorphous glassy polymer (Plexiglas). Note that the performance of Kevlar, aluminum, steel and Plexiglas were quantified from the macroscopic ballistic testing.⁵⁰ The outstanding behavior of SF films is attributed to the crystalline β -sheets to be the reinforcement fillers in an amorphous matrix and also the physical cross-links.¹¹ By virtue of the two-dimensional infinite sheet-like morphology of GO flakes, the 32 vol % nanocomposite considerably outperformed Kevlar, while not completely reaching the extrapolated value of single crystal multilayer graphene. This means that nanocomposites based on a finite size of GO flakes would potentially reach the antiballistic performance of the single crystal multilayer graphene through further interfacial optimization. Such optimization of spatial distribution of the filler and the interfacial interaction is completely plausible and paves the way for scaling up the nanocomposites.

To summarize, millimeter scale GO-SF nanocomposites were fabricated by SA-LbL assembly. The nanoscale structure, interfacial interactions between the components, and elastic modulus of the composite film was found to be highly dependent on the pH of the SF solution employed in the SA-

LbL assembly process. Microscopic ballistic characterization was conducted using high-velocity penetration of micro-sized projectiles through the nanocomposite films with different volume fractions of GO. Apart from the highly attractive features of GO-SF nacre-mimetic composites, such as layered architecture, precise control of thickness and spatial distribution of individual components, concerted hydrogen bonding, polar-polar, and hydrophobic interactions at the interface of GO and SF layers, our study strongly suggests that the nanoscale continuity of GO phase plays a critical role in the development of 2D nanomaterial-based composite armors. Therefore, the development of nanocomposite armors ought to be perused through the optimization of nanoscale morphologies and interactions of constituents with comprehensive HSR characterization. This work establishes a framework for HSR characterization of numerous nanocomposites that can be realized with natural and synthetic matrix and filler materials.

■ ASSOCIATED CONTENT

Supporting Information

The Supporting Information is available free of charge on the ACS Publications website at DOI: 10.1021/acs.nanolett.7b04421.

Experimental details including materials, preparation of graphene oxide flakes, preparation of silk fibroin, fabrication of GO-SF composite films, cross-sectional SEM of layer-by-layer GO-SF nanostructure, atomic

force microscopy, buckling test, microballistic testing, specific penetration energy, additional figures, table, and references (PDF)

AUTHOR INFORMATION

Corresponding Authors

*E-mail: (J.-H.L.) leejh@umass.edu.

*E-mail: (S.S.) singamaneni@wustl.edu.

ORCID

Wanting Xie: 0000-0002-0151-6362

Srikanth Singamaneni: 0000-0002-7203-2613

Jae-Hwang Lee: 0000-0002-2546-1044

Author Contributions

The authors W. X. and S. T. contributed equally to this work. The manuscript was written through contributions of all authors. All authors have given approval to the final version of the manuscript.

Author Contributions

The authors W.X. and S.T. contributed equally to this work. The authors would like thank Nanoresearch Facility and Institute of Materials Science and Engineering at Washington University for providing access to central microscopy facilities.

Funding

This research was supported by the U.S. Army Research Laboratory under contract W911NF-15-2-0024 and Air Force Office of Scientific Research under award # FA9550-15-1-0228.

Notes

The authors declare no competing financial interest.

REFERENCES

- (1) Sinha Ray, S.; Okamoto, M. *Prog. Polym. Sci.* **2003**, *28* (11), 1539–1641.
- (2) Podsiadlo, P.; Kaushik, A. K.; Arruda, E. M.; Waas, A. M.; Shim, B. S.; Xu, J. D.; Nandivada, H.; Pumphlin, B. G.; Lahann, J.; Ramamoorthy, A.; Kotov, N. A. *Science* **2007**, *318* (5847), 80–83.
- (3) Kim, H.; Abdala, A. A.; Macosko, C. W. *Macromolecules* **2010**, *43* (16), 6515–6530.
- (4) National Research Council. *Opportunities in protection materials science and technology for future Army applications*; National Academies Press, 2011; pp 24–34.
- (5) Kumar, N.; Kumbhat, S. *Essentials in Nanoscience and Nanotechnology*; John Wiley & Sons, Inc: Hoboken, New Jersey, 2016; pp 273–277.
- (6) Suk, J. W.; Piner, R. D.; An, J.; Ruoff, R. S. *ACS Nano* **2010**, *4* (11), 6557–6564.
- (7) Compton, O. C.; Nguyen, S. T. *Small* **2010**, *6* (6), 711–723.
- (8) Eda, G.; Fanchini, G.; Chhowalla, M. *Nat. Nanotechnol.* **2008**, *3* (5), 270–274.
- (9) Porter, D.; Vollrath, F. *Adv. Mater.* **2009**, *21* (4), 487–492.
- (10) Jin, H.-J.; Kaplan, D. L. *Nature* **2003**, *424* (6952), 1057–1061.
- (11) Jiang, C.; Wang, X.; Gunawidjaja, R.; Lin, Y. H.; Gupta, M. K.; Kaplan, D. L.; Naik, R. R.; Tsukruk, V. V. *Adv. Funct. Mater.* **2007**, *17* (13), 2229–2237.
- (12) Chen, F.; Porter, D.; Vollrath, F. *Acta Biomater.* **2012**, *8* (7), 2620–2627.
- (13) Hu, K.; Kulkarni, D. D.; Choi, I.; Tsukruk, V. V. *Prog. Polym. Sci.* **2014**, *39* (11), 1934–1972.
- (14) Kharlampieva, E.; Kozlovskaya, V.; Chan, J.; Ankner, J. F.; Tsukruk, V. V. *Langmuir* **2009**, *25* (24), 14017–14024.
- (15) Jiang, C.; Markutsya, S.; Tsukruk, V. V. *Adv. Mater.* **2004**, *16* (2), 157–161.
- (16) Vozar, S.; Poh, Y.-C.; Serbowicz, T.; Bachner, M.; Podsiadlo, P.; Qin, M.; Verploegen, E.; Kotov, N.; Hart, A. J. *Rev. Sci. Instrum.* **2009**, *80* (2), 023903.
- (17) Richardson, J. J.; Björnalm, M.; Caruso, F. *Science* **2015**, *348* (6233), aaa2491.
- (18) Chen, H.; Müller, M. B.; Gilmore, K. J.; Wallace, G. G.; Li, D. *Adv. Mater.* **2008**, *20* (18), 3557–3561.
- (19) Xu, Y.; Hong, W.; Bai, H.; Li, C.; Shi, G. *Carbon* **2009**, *47* (15), 3538–3543.
- (20) An, Z.; Compton, O. C.; Putz, K. W.; Brinson, L. C.; Nguyen, S. T. *Adv. Mater.* **2011**, *23* (33), 3842–3846.
- (21) Kharlampieva, E.; Kozlovskaya, V.; Wallet, B.; Shevchenko, V. V.; Naik, R. R.; Vaia, R.; Kaplan, D. L.; Tsukruk, V. V. *ACS Nano* **2010**, *4* (12), 7053–7063.
- (22) Hu, K.; Gupta, M. K.; Kulkarni, D. D.; Tsukruk, V. V. *Adv. Mater.* **2013**, *25* (16), 2301–2307.
- (23) Kulkarni, D. D.; Choi, I.; Singamaneni, S. S.; Tsukruk, V. V. *ACS Nano* **2010**, *4* (8), 4667–4676.
- (24) Yin, Y.; Hu, K.; Grant, A. M.; Zhang, Y.; Tsukruk, V. V. *Langmuir* **2015**, *31* (39), 10859–10870.
- (25) Wang, Y.; Ma, R.; Hu, K.; Kim, S.; Fang, G.; Shao, Z.; Tsukruk, V. V. *ACS Appl. Mater. Interfaces* **2016**, *8* (37), 24962–24973.
- (26) Tang, Z.; Kotov, N. A.; Magonov, S.; Ozturk, B. *Nat. Mater.* **2003**, *2* (6), 413–418.
- (27) Podsiadlo, P.; Liu, Z.; Paterson, D.; Messersmith, P. B.; Kotov, N. A. *Adv. Mater.* **2007**, *19* (7), 949–955.
- (28) Li, X.; Chang, W. C.; Chao, Y. J.; Wang, R.; Chang, M. *Nano Lett.* **2004**, *4* (4), 613–617.
- (29) Li, X.; Xu, Z. H.; Wang, R. *Nano Lett.* **2006**, *6* (10), 2301–2304.
- (30) Burghard, Z.; Zini, L.; Srot, V.; Bellina, P.; van Aken, P. A.; Bill, J. *Nano Lett.* **2009**, *9*, 4103–4108.
- (31) Xu, Z. H.; Li, X. *Adv. Funct. Mater.* **2011**, *21* (20), 3883–3888.
- (32) Xia, W.; Ruiz, L.; Pugno, N. M.; Keten, S. *Nanoscale* **2016**, *8* (12), 6456–6462.
- (33) Xia, W.; Song, J.; Meng, Z.; Shao, C.; Keten, S. *Mol. Syst. Des. Eng.* **2016**, *1* (1), 40–47.
- (34) El-Magd, E. J. *Phys. IV* **1994**, *4* (C8), C8-149–C8-170.
- (35) Radford, D. D.; Walley, S. M.; Church, P.; Field, J. E. *J. Phys. IV* **2003**, *110*, 263–268.
- (36) Al-Mousawi, M. M.; Reid, S. R.; Deans, W. F. *Proc. Inst. Mech. Eng., Part C* **1997**, *211* (4), 273–292.
- (37) Sarva, S.; Mulliken, A. D.; Boyce, M. C. *Int. J. Solids Struct.* **2007**, *44* (7–8), 2381–2400.
- (38) Watson, S.; Gifford, M.; Field, J. E. *J. Appl. Phys.* **2000**, *88* (1), 65–69.
- (39) Lee, J.-H.; Veyssset, D.; Singer, J. P.; Retsch, M.; Saini, G.; Pezeril, T.; Nelson, K. A.; Thomas, E. L. *Nat. Commun.* **2012**, *3* (May), 1164.
- (40) Lee, J.-H.; Loya, P. E.; Lou, J.; Thomas, E. L. *Science* **2014**, *346* (6213), 1092–1096.
- (41) Thevamaran, R.; Lawal, O.; Yazdi, S.; Jeon, S.-J. J.; Lee, J.-H.; Thomas, E. L. *Science* **2016**, *354* (6310), 312–316.
- (42) Tadepalli, S.; Hamper, H.; Park, S. H.; Cao, S.; Naik, R. R.; Singamaneni, S. *ACS Biomater. Sci. Eng.* **2016**, *2*, 1084.
- (43) Stafford, C. M.; Harrison, C.; Beers, K. L.; Karim, A.; Amis, E. J.; VanLandingham, M. R.; Kim, H.-C.; Volksen, W.; Miller, R. D.; Simonyi, E. E. *Nat. Mater.* **2004**, *3* (8), 545–550.
- (44) Genzer, J.; Groenewold, J. *Soft Matter* **2006**, *2* (4), 310.
- (45) Singamaneni, S.; Tsukruk, V. V. *Soft Matter* **2010**, *6* (22), 5681.
- (46) Shulha, H.; Po Foo, C. W.; Kaplan, D. L.; Tsukruk, V. V. *Polymer* **2006**, *47* (16), 5821–5830.
- (47) Cho, J.; Char, K.; Hong, J.-D.; Lee, K.-B. *Adv. Mater.* **2001**, *13* (14), 1076–1078.
- (48) Affdl, J. C.; Kardos, J. L. *Polym. Eng. Sci.* **1976**, *16*, 344–352.
- (49) Sadeghzadeh, S. *Appl. Phys. A: Mater. Sci. Process.* **2016**, *122* (7), 655.
- (50) Lee, B. L.; Walsh, T. F.; Won, S. T.; Patts, H. M.; Song, J. W.; Mayer, A. H. *J. Compos. Mater.* **2001**, *35* (18), 1605–1633.